

Dark Matter distribution in the Milky Way: microlensing and dynamical constraints

Fabio Iocco,¹ Miguel Pato,² Gianfranco Bertone,^{1,2} and Philippe Jetzer²

¹*Institut d'Astrophysique de Paris, UMR 7095-CNRS,
Univ. Pierre & Marie Curie, 98bis Bd Arago 75014 Paris, France*

²*Institute for Theoretical Physics, University of Zürich, Winterthurerstrasse 190, 8057 Zürich CH
(Dated: July 23, 2022)*

We show that current microlensing and dynamical observations of the Galaxy allow to set interesting constraints on the Dark Matter local density and profile slope towards the galactic centre. Assuming state-of-the-art models for the distribution of baryons in the Galaxy, we find that the most commonly discussed Dark Matter profiles (*viz.* Navarro-Frenk-White and Einasto) are consistent with microlensing and dynamical observations, while extreme adiabatically compressed profiles are robustly ruled out. When a baryonic model that also includes a description of the gas is adopted, our analysis provides a determination of the local Dark Matter density, $\rho_0 = 0.20 - 0.55 \text{ GeV/cm}^3$ at 1σ , that is found to be compatible with estimates in the literature based on different techniques.

I. INTRODUCTION

The presence of large amounts of Dark Matter (DM) in the Universe, and in particular in the Milky Way, is established on sound observational grounds [1–3]. However, a detailed description of the Dark Matter distribution in the Galaxy is hard to achieve, despite the tremendous progress in numerical simulations of galaxy-sized objects over the last few years [4–7], therefore precluding, among other things, a precise interpretation of direct and indirect Dark Matter searches (see e.g. Refs. [8–13]). In order to constrain Milky Way mass models, several observables have been used in the literature, including star counts, the motion of gas and stars or microlensing events. Here, we focus on two key probes, *viz.* microlensing observations and dynamical measurements, and show that interesting constraints can be set on the DM distribution using those measurements only. This provides complementary evidence for the existence of Dark Matter in the Galaxy, with a distribution compatible with that inferred from other observables.

Gravitational microlensing has long been adopted as a tool to study the structure of the Galaxy [14, 15]. This technique was suggested in [14] to probe the existence of Massive Compact Halo Objects (MACHOs) by using source stars in the Magellanic Clouds, M31 and M33. Soon after the observation of the first microlensing events in the early 90s [16–18], it became apparent that MACHOs could not be a dominant component of the galactic dark halo [19] – therefore a type of dark, non-compact matter was needed. Meanwhile, microlensing of stars towards the galactic centre proved useful in tuning the existent bulge, bar and disk models. Until today, several thousands of microlensing events have been collected – most notably by OGLE [18, 20, 21], MACHO [16, 22, 23], EROS [17, 24–26] and MOA [27] campaigns (see [28] for a review) – allowing for precise estimates of the microlensing optical depth towards the galactic bulge, spiral arms and Magellanic Clouds.

Another well-known tool to constrain the different components of our Galaxy is the rotation curve. Un-

like microlensing – which is sensitive to the distribution of compact matter along the line of sight –, dynamical measurements constrain the total mass distribution. Several decades ago, the observation of flat rotation curves in external spiral galaxies provided convincing evidence for Dark Matter, but actually the rotation curve of the Milky Way (a spiral itself) is far from being precisely determined given our peculiar position within the galactic disk. In fact, although hosts of data have been gathered over the years [29], allowing for ever more accurate dynamical models, sizeable uncertainties remain on Milky Way mass models, a circumstance that in turn affects our capability to constrain the DM distribution, as we shall see below.

In a pioneering work [30], Kuijken pointed out that a non-zero microlensing optical depth towards the galactic bulge sets a lower limit on the enclosed baryonic mass and thus a lower limit on the corresponding circular velocity within the solar circle. Using this result, Binney & Evans [31] derived an upper limit on the dark matter contribution to the rotation curve, which led them to the conclusion that “the cuspy haloes favoured by the Cold Dark Matter cosmology (and its variants) are inconsistent with the observational data on the Galaxy” [31]. This claim was however based on a preliminary determination of the microlensing optical depth by the MACHO collaboration [32] (later replaced by a less constraining measurement from the same collaboration [23]) as well as a very simplified treatment of the galactic rotation curve.

Here, we revisit this claim in light of recent microlensing observations towards a variety of galactic regions and up-to-date measurements of our Galaxy’s rotation curve. A very significant improvement of our work with respect to the existing literature is a proper inclusion of all experimental uncertainties regarding both microlensing and dynamical data, which makes our conclusions sound on statistical grounds. Furthermore, we shall also use a wide range of state-of-the-art models for the galactic baryonic component, so that modelling uncertainties are appropriately bracketed. Our ultimate aim is to combine microlensing and dynamical observables to draw robust

constraints on the Dark Matter distribution in the inner region of the Milky Way.

II. MILKY WAY MODELLING

In order to extract useful constraints on the DM distribution from microlensing and dynamical observables, we need to specify a mass model for our Galaxy. In this work, we shall implement a bulge/bar region, a disk and a Dark Matter halo. The Sun sits on the galactic disk at $(x_\odot, y_\odot, z_\odot) = (R_0, 0, 0)$, where R_0 is the galactocentric distance¹. We consider the range $R_0 = 8.0 \pm 0.5$ kpc throughout the analysis, taking 8.0 kpc as our fiducial value. This encompasses recent [34] and less recent [35] determinations as well as the 1985 IAU recommended values [36]. All scale distances in this Section are rescaled as $R_0/8$ kpc.

The bulge at the centre of the Milky Way has long been suspected to be bar-shaped. This was confirmed by near-infrared observations [37] and the distribution of red clump giant stars [38, 39], which produce convincing evidence for a triaxial bulge with its near end at positive galactic longitudes $\ell > 0$ and its major axis inclined $\alpha_b \sim 25^\circ$ with respect to the galactic centre line of sight. Several families of triaxial mass density distributions have been tested against the data, and two parameterisations appear to work particularly well [37, 38]:

$$\rho_b(x, y, z) = \rho_{0,b} e^{-r_1} \quad (\text{E2}) \quad (1)$$

$$\rho_b(x, y, z) = \rho_{0,b} e^{-\frac{r_2^2}{2}} \quad (\text{G2}) \quad , \quad (2)$$

with

$$r_1^2 = \frac{x'^2}{x_b^2} + \frac{y'^2}{y_b^2} + \frac{z'^2}{z_b^2}, \quad r_2^4 = \left(\frac{x'^2}{x_b^2} + \frac{y'^2}{y_b^2} \right)^2 + \frac{z'^4}{z_b^4} \quad ,$$

where (x', y', z') are the coordinates along the major, intermediate and minor axes, respectively, and the parameters of these fitting formulae are [38]

$$\text{E2: } \alpha_b = 23.8^\circ; (x_b, y_b, z_b) = (0.899, 0.386, 0.250) \frac{R_0}{8 \text{ kpc}} \text{ kpc}$$

$$\text{G2: } \alpha_b = 24.9^\circ; (x_b, y_b, z_b) = (1.239, 0.609, 0.438) \frac{R_0}{8 \text{ kpc}} \text{ kpc}.$$

For both the E2 and G2 models, we implement an exponential cutoff proportional to $\exp(-(R' - R_m)^2/2r_0^2)$ (with $R'^2 = x'^2 + y'^2$, $r_0 = 0.5$ kpc) beyond the corotation radius $R_m = 3.5$ kpc as in [37, 40]. Another

relevant bulge model is the one introduced by Zhao in [41],

$$\rho_b(x, y, z) = \rho_{0,b} \left(s_a^{-1.85} e^{-s_a} + e^{-\frac{r_2^2}{2}} \right) \quad (\text{Zhao}) \quad , \quad (3)$$

with $s_a^2 = (q_b^2(x^2 + y^2) + z^2)/z_b^2$, which is particularly suited to produce a steep rise in the rotation curve at $r \lesssim 0.5$ kpc. Inspired by [42] we shall consider an axisymmetrised version of this profile with $x_b = y_b = 0.9$ kpc($R_0/8$ kpc), $z_b = 0.4$ kpc($R_0/8$ kpc) and $q_b = 0.6$. Finally, the recent and sophisticated model of Gardner et al [43, 44] is also implemented – in this case there are separate bar and bulge components:

$$\rho_b(x, y, z) = f_{0,b} (\rho_{bar}(x, y, z) + \rho_{bulge}(x, y, z)) \quad (4)$$

(Gardner et al) ,

where the bar density is given by a Ferrers model [45]

$$\rho_{bar}(x, y, z) = \begin{cases} \rho_{0,bar} (1 - r_1^2)^n & \text{for } r_1 < 1 \\ 0 & \text{for } r_1 \geq 1 \end{cases} \quad ,$$

with $n = 2$, $\alpha_b = 25^\circ$, $x_b = 3.5$ kpc($R_0/8$ kpc), $y_b = 1.4$ kpc($R_0/8$ kpc), $z_b = 1.0$ kpc($R_0/8$ kpc), $M_{bar} = 10^{10} M_\odot$ [43], and the bulge component is given in terms of the gravitational potential ϕ_{bulge} defined in [44]. The mass density associated to ϕ_{bulge} is readily obtained using the Poisson equation. The constant $f_{0,b}$ is just a normalisation and its role will become apparent in Section III.

As for the stellar disk in our Galaxy, it is well-known that there are a thin and a thick components corresponding to distinct star populations. Instead of covering a whole range of different vertical and radial disk profiles, we adopt two extreme cases: a thin-only disk and a thin+thick disk. Although the former model is somewhat unrealistic, it will prove useful in exploring the present uncertainty associated to disk modelling. Following [40, 46],

$$\rho_d(R, z) = \frac{\rho_{0,d}}{\eta} e^{-\frac{R-R_0}{H}} \left[(1 - \beta) \text{sech}^2 \frac{z}{\eta h_1} + \beta e^{-\frac{|z|}{\eta h_2}} \right] \quad (5)$$

(Han & Gould)

with

$$R^2 = x^2 + y^2, \quad H = 2.75 \frac{R_0}{8 \text{ kpc}} \text{ kpc},$$

$$h_1 = 0.270 \frac{R_0}{8 \text{ kpc}} \text{ kpc}, \quad h_2 = 0.440 \frac{R_0}{8 \text{ kpc}} \text{ kpc},$$

$$\eta(R) = \max \left[0.670, 0.114 + \frac{R}{9.025 \text{ kpc}} \right]$$

$$\text{thin: } \beta = 0, \quad \rho_{0,d} = 4.4 \times 10^7 \eta(R_0) M_\odot/\text{kpc}^3$$

$$\text{thin+thick: } \beta = 0.565, \quad \rho_{0,d} = 4.93 \times 10^7 M_\odot/\text{kpc}^3.$$

Again, we shall also refer to the model of Gardner et al where both stellar and gas disks are modelled through

¹ Actually, the Sun lies somewhat off the central plane at $z_\odot \lesssim 30$ pc [33], but this is a very small displacement compared to other quantities at play and thus we shall take the reasonable assumption $z_\odot = 0$.

the corresponding gravitational potentials (see details in [44]).

In the remainder of the work, five models for the galactic baryonic component (i.e. bulge/bar and disk) will be used:

- **Model 1:** E2 bulge and thin+thick disk;
- **Model 2:** G2 bulge and thin+thick disk;
- **Model 3:** G2 bulge and thin disk;
- **Model 4:** Zhao bulge and thin disk; and
- **Model 5:** Gardner et al bulge/bar, stellar disk and gas disk.

We emphasise that these fiducial setups reasonably bracket the uncertainties in modelling the galactic baryonic component, and thus will be useful in assessing how our results depend on such modelling.

The last piece missing in our Milky Way mass model is the Dark Matter halo. In view of the findings of numerical simulations [4, 6], we implement spherically symmetric generalised Navarro-Frenk-White (NFW) and Einasto profiles:

$$\rho_{DM}(r) = \bar{\rho}_s (r/r_s)^{-\alpha} (1 + r/r_s)^{-3+\alpha} \quad (\text{NFW}) \quad (6)$$

$$\rho_{DM}(r) = \bar{\rho}_s \exp \left[-\frac{2}{\alpha} \left(\left(\frac{r}{r_s} \right)^\alpha - 1 \right) \right] \quad (\text{Einasto}), \quad (7)$$

where $r^2 = x^2 + y^2 + z^2$, r_s is the scale radius, $\bar{\rho}_s$ is the scale density and α is the inner slope for the NFW profile and a shape parameter for the Einasto profile. Typical ranges found in N -body simulations are $0.9 \lesssim \alpha \lesssim 1.2$ in the case of NFW [4, 47] and $0.12 \lesssim \alpha \lesssim 0.22$ in the case of Einasto [47–50]. In the following, the normalisation of the DM profile will be set by the local DM density, $\rho_0 \equiv \rho_{DM}(R_0)$, that can be easily cast in terms of $\bar{\rho}_s$. We shall take a fiducial interval $\rho_0 = 0.4 \pm 0.1 \text{ GeV/cm}^3$ in line with recent determinations [42, 51, 52].

Regarding the scale radius r_s , DM-only simulations tell us that the virial concentration $c_{vir} = r_{vir}/r_s$ of an object of mass $M_{vir} = 10^{12} h^{-1} M_\odot$ lies in the range $\log_{10} c_{vir} = 0.9 - 1.1$ (at 1σ) [53] which translates into $r_s \sim 24 - 38 \text{ kpc}$. However, works where galactic dynamical observables are used to constrain a Milky Way mass model [42] (see also [54]) seem to favour higher concentrations, $c_{vir} = 10 - 25$, or $r_s \sim 12 - 30 \text{ kpc}$. Hence, we shall take in the following a rather wide range $r_s = 20_{-10}^{+15} \text{ kpc}$.

We stress that the Dark Matter profiles found in numerical simulations deviate significantly from spherical symmetry: while DM-only simulations lead to very prolate shapes, the inclusion of baryons leads to more oblate (but still triaxial) DM distributions [55, 56]. In order to check the relevance of a non-spherical DM halo for our purposes, we shall also consider the NFW profile in equation (6) with r replaced by $m = (x^2 + y^2 + z^2/q^2)^{1/2}$ and axis ratio $q = 0.7$. This represents an oblate profile with a shape compatible with the results of [52].

As of today, it is not clear how baryons affect the DM profile in our Galaxy. One possibility is that when the Galaxy formed and the baryons contracted towards the centre, the dissipationless component was dragged leading to a steepening of the DM profile. This was proposed long ago in Ref. [57], where a simple adiabatic contraction model was introduced (more refined models have also been constructed, see Refs. [58, 59]): given a spherically symmetric initial total mass distribution $M_i(< r_i)$ and a final baryon distribution $M_b(< r)$, the final DM distribution $M_{DM}(< r)$ obeys [57]

$$r (M_b(< r) + M_{DM}(< r)) = r_i M_i(< r_i) \quad , \quad (8)$$

with $M_{DM}(< r) = (1 - f_b) M_i(< r_i)$, f_b being the total baryonic fraction in the Galaxy. Taking $M_i(< r_i)$ to be the initial mass distribution associated to the NFW profile (6) and $M_b(< r)$ the baryonic mass distribution given by models 1–5, we can easily solve (8) for r while fixing r_i and f_b . This sets the final mass distribution $M_{DM}(< r)$ and (upon derivation) the DM profile. For the sake of completeness, in our analysis we shall also use the described procedure to model the DM profile and therefore test adiabatic contraction models against galactic dynamical observables.

Finally, note that in the following, given a baryonic model and assumed r_s , we let vary ρ_0 and α . These will be the main phenomenological parameters in our analysis.

III. MICROLENSING

In this Section we present a brief overview of the gravitational microlensing formalism and of the most recent observations.

A. Theoretical framework

Gravitational microlensing is a direct consequence of Einstein's General Relativity: as a massive compact object – the lens – moves across the line of sight towards a given luminous source, the source light gets deflected and two distinct images form. In the microlensing regime these images are not resolved and hence the observable effect is a temporary magnification of the source. For a point-like source and a point-like lens, the magnification of the source reads [14]

$$A(t) = \frac{u(t)^2 + 2}{u(t) \sqrt{u(t)^2 + 4}} \quad , \quad (9)$$

where $u(t)$ is the transverse distance between the lens and the line of sight measured in units of the Einstein radius $R_E = \sqrt{(4GM_l/c^2) D_l (1 - D_l/D_s)}$. Here, D_l (D_s) is the distance between the observer and the lens (source) and M_l is the lens mass. The typical duration of a microlensing event is set by the Einstein radius and the lens velocity in the plane perpendicular to the line of sight v_T :

$t_E = R_E/v_T$. For galactic lens objects with masses ranging from $10^{-6} M_\odot$ to $10^2 M_\odot$, the typical microlensing time scale varies from a few hours to a few years [14]. Therefore, a thorough monitoring of galactic stars in different directions can be used to study a whole population of low-luminosity objects along the line of sight, which would otherwise remain undetected.

The probability of observing the microlensing of a given luminous source is driven by the mass distribution of lenses ρ_l along the line of sight. A particularly interesting quantity is the optical depth τ which quantifies the probability that a lens comes within one Einstein radius of the line of sight, or equivalently that the magnification of the source exceeds $A = 1.34$ (cf. equation (9) with $u = 1$). If all sources towards galactic coordinates (ℓ, b) are placed at the same distance D_s (we will relax this simplifying assumption for a more general formulation later on), the theoretically expected optical depth can be written as:

$$\tau(\ell, b, D_s) = \frac{4\pi G}{c^2} \int_0^{D_s} dD_l \rho_l(\ell, b, D_l) D_l \left(1 - \frac{D_l}{D_s}\right), \quad (10)$$

where ρ_l refers to all possible lens objects (in our case the bulge/bar and the stellar disk). For our purposes it is important to stress that (i) microlensing is caused only by massive compact bodies, and not by gas nor Dark Matter; and (ii) the optical depth τ is independent of the lens mass function, since the surface of the Einstein disk is proportional to M_l . As a consequence, measurements of the optical depth depend only on the line of sight integral of the mass density of lenses ρ_l as emphasised in equation (10), and will therefore set the normalisation of our baryonic models.

It is to be noted that equation (10) is obtained under the assumption that all the sources lie at the same distance D_s . This is no longer valid for microlensing observations towards the galactic centre, as self-lensing (caused by the fact that a “source” in a lensing event is also acting as lens for another event) plays an important role. In this case one has to integrate not only on the distance of the lenses but also on the distance of the sources, since the number density of both sources and lenses can vary substantially [15]:

$$\langle\tau\rangle(\ell, b) = \frac{\int_0^{r_\infty} dD_s \tau(\ell, b, D_s) dn_s/dD_s}{\int_0^{r_\infty} dD_s dn_s/dD_s}, \quad (11)$$

where $dn_s/dD_s \propto \rho_s(D_s)D_s^{2+2\beta_s}$ is the distance distribution of detectable sources, ρ_s is the mass density of sources and r_∞ is the maximum distance at which sources can be found that we fix to $r_\infty = 20$ kpc (our results do not depend much on the specific choice of this parameter). Notice that the expression for dn_s/dD_s , introduced in [15], includes both a volume effect in the D_s^2 factor since more sources lie at greater distances, and a luminosity effect in the factor $D_s^{2\beta_s}$ given that only sources above the threshold luminosity can be detected (assuming that the distribution of sources above luminosity L

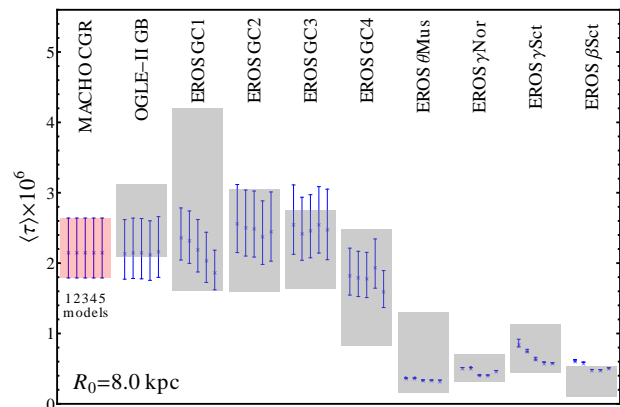


FIG. 1: Measured and expected microlensing optical depths for different galactic regions. The measured optical depths along with the corresponding uncertainties are shown by the boxes, while the expected values from our baryonic models are shown by the blue dots and error bars. All five models defined in Section II have been scaled to agree with the MACHO [23] measurement towards $(\ell, b) = (1.5^\circ, -2.68^\circ)$ represented by the leftmost box. Using this normalisation we show the expected optical depth for different fields of view observed by several campaigns: OGLE-II GB [21], EROS GC1-4 [25] and EROS θ Mus, γ Nor, γ Sct, β Sct [26]. In this plot all uncertainties are 1σ and $R_0 = 8$ kpc.

follows L^{β_s}). The index β_s depends, of course, on the type of source and it is usually taken to be $\beta_s \lesssim -1$ for main sequence stars and $\beta_s = 0$ for red giant clump stars [46, 60]. In the following Section we explain how we use ρ_s and ρ_l to recover the expected optical depth from each of the models defined in Section II, while comparing it with observations.

B. Observations

Early measurements of the optical depth towards the galactic bulge [22, 27, 32] showed values significantly higher than what expected from initial estimates [14, 15]. This motivated the study in [31], as previously discussed, in the then-justified belief that the higher density of lenses for microlensing would leave less room for the gas and Dark Matter components in our Galaxy. However, since those early measurements, huge progress has been done in microlensing observations and modelling of the bulge (see Section II for this latter point): in fact, the MACHO, EROS and OGLE collaborations have recently performed measurements of the optical depth towards the galactic centre. The present values are less constraining than the early results, thus making it compelling to perform a more accurate analysis of the different mass components of our Galaxy.

As a default, we start by adopting the 2005 measurement of the MACHO collaboration towards the galactic bulge [23]. Out of the 94 observed fields, they identify 9

at very small galactic latitude and longitude as the Central Galactic Region (CGR), and find the average value

$$\langle \tau \rangle = 2.17_{-0.38}^{+0.47} \times 10^{-6} \text{ for } (\ell, b) = (1.50^\circ, -2.68^\circ) \quad (12)$$

We scale our bulge models to meet this optical depth measurement as done in [40]: assigned all model parameters but $\rho_{0,b}$ for models 1–4 or $f_{0,b}$ for model 5, we set the latter by requiring that the opacity obtained using equation (11) matches the value in equation (12). We checked that our optical depth results for models 1 and 2 are in agreement with those obtained in Figure 1 of Ref. [40]. Since the source stars monitored in [23] are red clump giants in the galactic bulge, we fix $\beta_s = 0$ in equation (11) while using $\rho_s \equiv \rho_b$ and $\rho_l \equiv \rho_b + \rho_d$. Notice that this procedure gives an 1σ range for $\rho_{0,b}$ or $f_{0,b}$ corresponding to the experimental uncertainty in equation (12).

We repeat the procedure for each model discussed in Section II, thus fixing the galactic baryonic component. It is now possible to cross-check our models against current observations from other experimental groups. We do so by computing the optical depth through equation (11) making use of the just-defined bulge normalisations. In particular, we consider the following measurements:

- OGLE-II GB [21]: $\langle \tau \rangle = 2.55_{-0.46}^{+0.57} \times 10^{-6}$ for $(\ell, b) = (1.16^\circ, -2.75^\circ)$. In this case we use $\beta_s = 0$, $\rho_s \equiv \rho_b$ and $\rho_l \equiv \rho_b + \rho_d$ in equation (11) since the source stars are red clump giants in the galactic bulge.
- EROS GC1–4 [25]: $\langle \tau \rangle = 2.90 \pm 1.30 \times 10^{-6}$ for $(\ell, b) = (-4.5^\circ, 2.40^\circ)$; $\langle \tau \rangle = 2.32 \pm 1.73 \times 10^{-6}$ for $(\ell, b) = (-1.5^\circ, 2.42^\circ)$; $\langle \tau \rangle = 2.20 \pm 1.56 \times 10^{-6}$ for $(\ell, b) = (1.5^\circ, 2.22^\circ)$; $\langle \tau \rangle = 1.65 \pm 0.83 \times 10^{-6}$ for $(\ell, b) = (4.5^\circ, 2.53^\circ)$. In this case we use $\beta_s = 0$, $\rho_s \equiv \rho_b$ and $\rho_l \equiv \rho_b + \rho_d$ in equation (11) since the source stars are red clump giants in the galactic bulge.
- EROS spiral arms [26]: $\langle \tau \rangle = 0.67_{-0.52}^{+0.63} \times 10^{-6}$ for $(\ell, b) = (306.56^\circ, -1.46^\circ)$ θ Mus; $\langle \tau \rangle = 0.49_{-0.18}^{+0.21} \times 10^{-6}$ for $(\ell, b) = (331.09^\circ, -2.42^\circ)$ γ Nor; $\langle \tau \rangle = 0.72_{-0.28}^{+0.41} \times 10^{-6}$ for $(\ell, b) = (18.51^\circ, -2.09^\circ)$ γ Sct; $\langle \tau \rangle = 0.30_{-0.20}^{+0.23} \times 10^{-6}$ for $(\ell, b) = (26.60^\circ, -2.15^\circ)$ β Sct. In this case we use $\rho_l \equiv \rho_b + \rho_d$ in equation (11) and replace dn_s/dD_s by a gaussian of mean 7 kpc and standard deviation 1 kpc in good agreement with the source distance distribution shown in Figure 11 of Ref. [26].

The results of this cross-check are presented in Figure 1, where the boxes represent the experimental measurements and corresponding 1σ uncertainties, while the blue dots and error bars refer to the theoretical expectations of the five baryonic models once normalised to the MACHO CGR result in equation (12). It is evident that we obtain a very good agreement for all models, since the expected ranges fall nicely within less than 1σ off the

measurements, the only exceptions being models 1 and 2 for the spiral arm β Sct (but in this case the discrepancy is just slightly above 1σ and so we shall not consider it worrying). This is in fact a reassuring result.

Notice that we reproduce the experimental results not only in the innermost galactic fields reached by OGLE-II [21] and EROS [25], but also beyond the limits of the central galactic regions where EROS collected microlensing events from four spiral arms across the sky [26]. It is hence fair to state that the five models defined in Section II and normalised to 2005 MACHO optical depth in equation (12) are in good agreement with present microlensing data. Moreover, we have further checked that the corresponding bulge masses are well within the values found in literature $M_b \simeq 1 - 2 \times 10^{10} M_\odot$ [37, 40, 61, 62]. We shall use these five models in the remainder of the present work.

Several comments are in order here. First, let us stress that all microlensing data used up to now (including the 2005 MACHO result [23], which is the one adopted throughout our analysis) are sensitive to Einstein times $3 \lesssim t_E/\text{days} \lesssim 700$, or in lens masses $1.4 \times 10^{-3} \lesssim M_l/M_\odot \lesssim 79$ (in this simple estimate we have assumed the typical values $v_T = 100$ km/s, $D_s = 10$ kpc and $D_l = 0.5D_s$). This means that compact, baryonic objects of virtually all masses (including all stars and the most massive planets) contribute to the observed optical depth to which we are normalising our bulge models.

In particular, less massive planets ($M_l/M_\odot \lesssim 1.4 \times 10^{-3}$) could also contribute significantly to the galactic mass budget, and one might wonder whether the population of unbound Jupiter-mass objects recently discovered through microlensing [63] could lead to a systematic underestimate of the baryonic model normalisation. The presence of these objects has been invoked to explain MOA and OGLE microlensing events with $t_E < 2$ days, and their abundance has been estimated to be approximately twice that of main-sequence stars [63]. Their contribution to the mass density in the bulge/bar and disk is

$$f_{\text{PL}} = \frac{\int dM M (dN/dM)_{\text{PL}}}{\int dM M (dN/dM)_{\text{stars}}} \quad , \quad (13)$$

where $(dN/dM)_{\text{PL}}$ and $(dN/dM)_{\text{stars}}$ are the mass functions of the Jupiter-mass population and the stars, respectively. Taking a Dirac delta for $(dN/dM)_{\text{PL}}$ and model 1 of Table S3 of the supplementary information of Ref. [63], we find $f_{\text{PL}} \simeq 0.1\%$. We shall therefore neglect this newly discovered population in our calculations, since its contribution is much smaller than the uncertainties in the mass model.

IV. ROTATION CURVE

This Section is dedicated to outlining the formalism and observational status regarding one key dynamical observable, the galactic rotation curve.

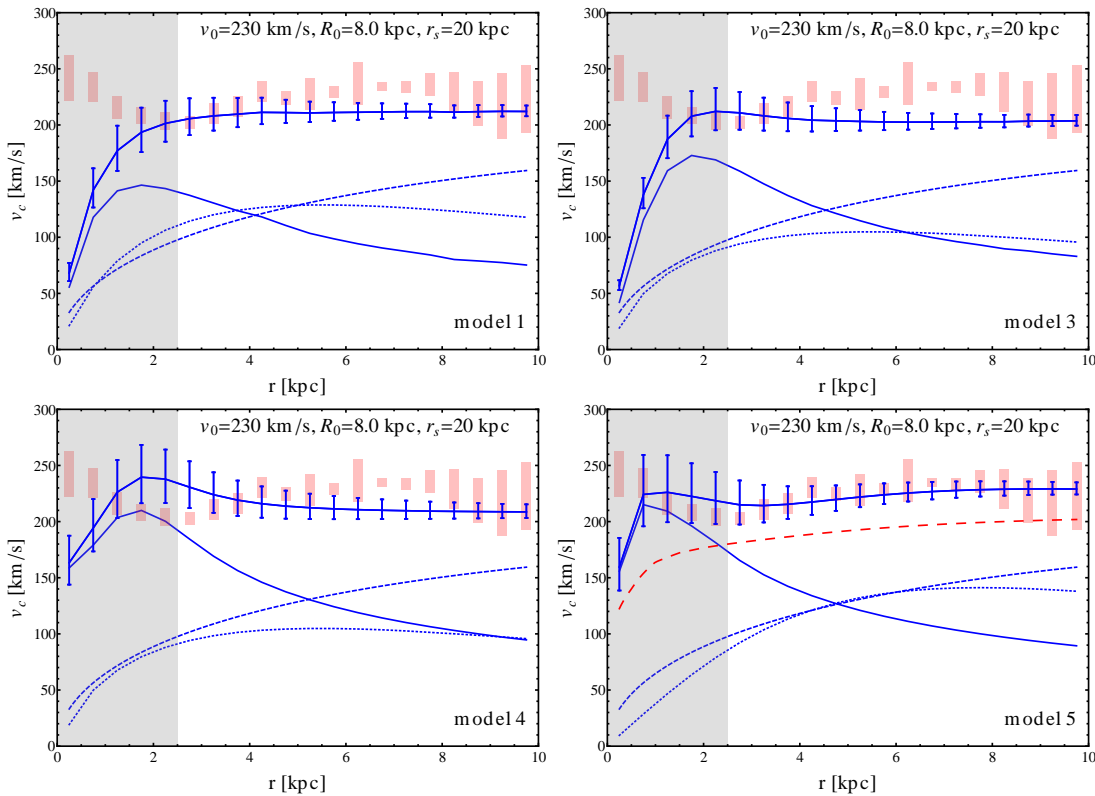


FIG. 2: The break-down of the rotation curve $v_c(r)$ for different Milky Way mass models. The lower solid, dotted and dashed lines correspond to the individual contributions of bulge/bar, disk and halo, respectively. In all frames the adopted Dark Matter halo follows a spherical NFW profile with $r_s = 20$ kpc, $\alpha = 1$ and $\rho_0 = 0.4$ GeV/cm³. The rotation curve for model 2 has been omitted since it is very similar to the one featured in model 1. The upper blue solid line with error bars indicates the expected total rotation curve, while the red (dark) boxes show the compilation of data in [29] rescaled to $R_0 = 8$ kpc and $v_0 = 230$ km/s. The leftmost shaded area shows the cut $r \geq 2.5$ kpc used throughout the analysis. The red long-dashed line in the bottom right frame shows the adiabatic compression of an initial NFW profile with $r_s = 20$ kpc, $\alpha = 1$ and $\rho_0 = 0.4$ GeV/cm³ and assuming model 5 for the baryonic mass distribution. In these plots all uncertainties are 1σ .

A. Theoretical framework

Regardless of their nature, all forms of *matter* contribute to the rotation curve of our Galaxy, unlike the case of microlensing, where only compact bodies along the line of sight play a role. This is basically what allows us to extract information about the DM and gas components. In full generality, the circular velocity v_c at a given galactocentric distance r reads

$$v_c^2(r) = \sum_i v_{c,i}^2(r) = \sum_i r \frac{d\phi_i}{dr}(r, \theta = \pi/2, \varphi) \quad , \quad (14)$$

where i runs over all the mass components (bulge/bar, disk and Dark Matter halo), ϕ_i is the gravitational potential associated to component i and (r, θ, φ) are galactic spherical coordinates ($\theta = \pi/2$ defines the plane of the galactic disk). For the spherical Dark Matter halos in equations (6) and (7) one recovers the well-known expression $v_{c,DM}^2(r) = GM_{DM}(< r)/r$, where $M_{DM}(< r)$ is the DM mass enclosed in a sphere of radius r around the galactic centre. The case of an oblate halo referred to

at the end of Section II can also be treated analytically with a slightly more complicated expression (cf. equation (2-91) in [64]). As for the baryonic contribution, let us notice that all components of model 5 are specified through their gravitational potential, which renders trivial the computation of the corresponding circular velocity with equation (14). Finally, since the mass distributions of models 1–4 are rather complicated and triaxial in general, there is no simple expression for v_c ; in this case we compute the gravitational potential due to an arbitrary mass distribution by expressing the solution of the Poisson equation as a series of multipoles up to order $l_{max} = 2$ (cf. equation (2-122) in [64]) and then apply equation (14). All theoretical expectations for v_c presented in the following have been averaged over φ in order to ease comparison with experimental data (which refer to different positions across the galactic plane).

With this formalism at hand we can finally compute the rotation curve associated to the different models specified in Section II and whose bulge/bar components were appropriately normalised to microlensing data (see Section III and Figure 1 for details). Figure 2 displays the

rotation curve break-down for our baryonic models (models 1 and 2 yield very similar rotation curves despite the different bulge shapes, so we omit the latter model for plotting purposes) and selecting a spherical NFW profile with $r_s = 20$ kpc, $\alpha = 1$ and $\rho_0 = 0.4$ GeV/cm³. The bulge/bar, disk and halo contributions are represented by the lower solid, dotted and dashed curves, respectively, in the range $r = 0 - 10$ kpc with bins of 0.5 kpc. Notice that for model 5 the disk contribution in dotted contains both the stellar and gas components. The upper blue solid curve with error bars in every frame of Figure 2 denotes the total rotation curve predicted by each model. The error bars show the propagated uncertainty due to the bulge normalisation scaled to MACHO microlensing optical depth in equation (12). As we shall see, the combination of microlensing data and the rotation curve sets an upper limit on the distribution of Dark Matter across the Galaxy. Before deriving these constraints, we turn to the status of present data on the galactic rotation curve, represented by the red (dark) boxes in Figure 2.

B. Observations

Different methods are available to infer the galactic rotation curve at galactocentric distances $r \lesssim 10$ kpc, which is the range we are interested in for the scope of this paper. One of the most used techniques relies on the observation of gas clouds moving in the galactic plane. For each line of sight (ℓ, b) the extreme velocity v_t – the so-called “terminal velocity” – is measured and converted to the circular velocity at a given radius under the assumption of strictly circular gas orbits [65]: $v_c(R_0 \sin \ell) = v_t(\ell) + v_0 \sin \ell$, where $v_0 \equiv v_c(R_0)$ is the local circular velocity. The 21 cm line is widely used in literature to determine the terminal velocity of gas clouds in the inner regions of the Milky Way. Other kinematical probes for the outer regions of our Galaxy are C-stars, observed through near-infrared photometry (e.g. [66]), and the CO emission line of HII regions (e.g. [67]).

Generically, the observed velocities of either gas clouds or stars with respect to the Earth must be transformed to a circular velocity through specific assumptions on the local reference frame. The different values adopted by the several observational groups over the years make it difficult to simply take their final values altogether. In Ref. [29] the authors construct a rotation curve of the Galaxy starting from the very observational data, and unify the inference of rotation curves for a single set of local galactocentric radius and local circular velocity $(R_0, v_0) = (8.0 \text{ kpc}, 200 \text{ km/s})$. Here we use that compilation of data, which includes measurements from several observational groups and techniques.

The values of (R_0, v_0) adopted in the literature vary significantly, and since the constraints we shall obtain in Section V depend quite sensitively on the choice of the Earth reference frame, we will take into account the error on R_0 and v_0 throughout the analysis in order to

“bracket” the uncertainty on the constraints. In addition to the range $R_0 = 8.0 \pm 0.5$ kpc mentioned in Section II, we consider local circular velocities in the interval $v_0 = 230 \pm 30$ km/s. This choice reasonably encompasses a broad set of measurements [68–72]. Recent analyses (e.g. [70]) in particular seem to indicate local velocities well in excess of the 1985 IAU recommended value $v_0 = 220$ km/s [36]. In order to convert the data in [29] to a given set (R'_0, v'_0) , the following transformation laws are applied:

$$R' = R \frac{R'_0}{R_0} \quad ; \quad v'_t = v_t + \frac{R}{R_0}(v'_0 - v_0) \quad (15)$$

with the *primed* quantities being the ones obtained with our new choice of (R'_0, V'_0) , and the *plain* ones being those as from [29], with $(R_0, v_0) = (8.0 \text{ kpc}, 200 \text{ km/s})$. These transformation laws are only strictly valid for the measurement of terminal velocities. However, since our constraints will come essentially from radii within the Solar circle, where terminal velocity data points dominate the compilation in Ref. [29], this procedure is reasonable.

Given that we are using a compilation of data obtained with different techniques, the treatment of uncertainties on the derived quantity $v_c(r)$ is a delicate matter. The following strategy is adopted in this work. After scaling the data from [29] to a given (R_0, v_0) according to equations (15), a binning of 0.5 kpc is applied in the galactocentric distance range $r = 0 - 10$ kpc. Since several measurements lie in each r -bin, the central value on v_c is taken to be the mean of all the central values in the bin, while the corresponding 1σ systematic uncertainty is the standard deviation of the central values. We estimate the 1σ statistical uncertainty as the mean of the 1σ uncertainties of all the measurements in each bin, and add it to the systematic error. It is this total uncertainty that is represented by the red (dark) boxes in Figure 2 (for $R_0 = 8$ kpc, $v_0 = 230$ km/s) and that we use to gauge our knowledge on the Milky Way rotation curve in the following Section.

We restrict our analysis to galactic radii $r \geq 2.5$ kpc, corresponding to longitudes $|\sin \ell| \geq 0.30 - 0.35$ in line with what is usually done in the literature [42, 62]. This cut – marked in the plots of Figure 2 – is imposed by the severe triaxiality of the gravitational potential in the inner galactic regions caused by the presence of the galactic bar, invalidating the assumption of circular orbits.

V. RESULTS

We now turn to the discussion of our results. From Figure 2 one can see how the modelling of the baryonic component in our Galaxy affects the rotation curve. First of all, let us recall that the expected circular velocity depicted in that Figure is obtained by tuning our bulge models to microlensing data, independently of the data on the rotation curve itself. It is thus remarkable that in all frames the expectation roughly matches the data –

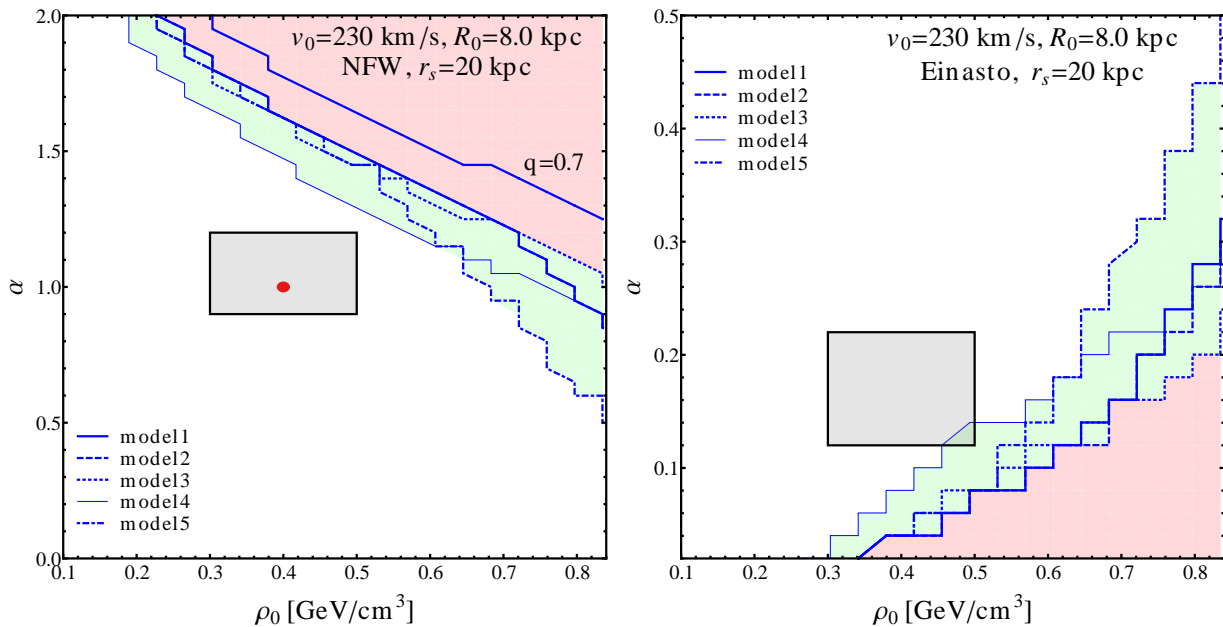


FIG. 3: Constraints on the Dark Matter distribution parameters ρ_0 and α provided by current data on the Milky Way rotation curve for a generalised NFW (left) and an Einasto (right) profile. The thick solid, thick dashed, thick dotted, thin solid and thick dot-dashed lines are the 2σ constraints in the case where the galactic baryonic component follows model 1, 2, 3, 4 and 5, respectively, all scaled to match the microlensing optical depth in equation (12). The green (light) shadowed area delimits the uncertainty on the constraint given the present-day baryonic models, while the red (dark) shadowed region indicates the excluded parameters. In the left frame, the upper thick solid line labelled “ $q = 0.7$ ” refers to the constraints for an oblate NFW profile with axis ratio $q = 0.7$ in the case of taking model 1 for the baryonic component. The shadowed rectangle encompasses the ranges of profile slopes found in numerical simulations and the values of ρ_0 found in the recent literature (see Section II), while the red filled circle in the left frame marks the parameter set ($\rho_0 = 0.4 \text{ GeV/cm}^3, \alpha = 1.0$) used to produce Figure 2. In both frames we have fixed $r_s = 20 \text{ kpc}$, $R_0 = 8.0 \text{ kpc}$ and $v_0 = 230 \text{ km/s}$.

this argues in favour of the accurateness of present Milky Way mass models in explaining both microlensing and dynamical observables. Models 1–4, in particular, succeed in reproducing a flat rotation curve for $r \gtrsim 2.5 \text{ kpc}$ but appear slightly below the data at $6 \text{ kpc} \lesssim r \lesssim 10 \text{ kpc}$, while model 5 does feature the exact same pattern indicated by the data. Again, we shall not regard the inner 2.5 kpc to set our constraints.

Notice as well that the coarse r -binning may be misleading at small scales; model 5, for instance, produces a steep bump in v_c at $r \lesssim 0.5 \text{ kpc}$ (see e.g. Ref. [44]) which is not seen in Figure 2 simply because of the chosen bins.

A. Conservative constraints on (ρ_0, α)

Figure 2 assumes an NFW profile with fiducial values $\rho_0 = 0.4 \text{ GeV/cm}^3$, $\alpha = 1.0$ (and $r_s = 20 \text{ kpc}$). We are now interested in studying the constraints that can be set in the DM parameter space (ρ_0, α) by using the data on the Milky Way rotation curve. A given set (ρ_0, α) will be considered to be excluded at 2σ if in any radial bin in the range $2.5 \text{ kpc} \leq r \leq 10 \text{ kpc}$ the 2σ lower end of the expected v_c (curve with error bars in Figure 2) exceeds the 2σ upper end of the measured v_c (boxes in Figure 2). This is a rather conservative procedure indeed – note,

for instance, that for model 4 the fiducial NFW setup (see bottom left frame of Figure 2) is not excluded at 2σ , even though the predicted rotation curve is far from explaining the data.

The constraints obtained with these definitions are shown in Figure 3 for the different models 1–5 and the generalised NFW (left) and Einasto (right) DM profiles. Red (dark) shading signals the excluded regions and green (light) shading spans the uncertainty on the exact constraint given the present-day baryonic models. These plots assume the fiducial setup $r_s = 20 \text{ kpc}$, $R_0 = 8.0 \text{ kpc}$, $v_0 = 230 \text{ km/s}$. It is worth mentioning that the constraints presented in Figure 3 are generally dominated by two radial bins: the one centred at $r = 2.75 \text{ kpc}$ for small local DM densities and the one at $r = 7.75 \text{ kpc}$ for larger densities.

The conservative constraints shown in Figure 3 are found to be consistent with the range of inner slopes/shape parameters α found in numerical simulations and local DM densities ρ_0 hinted by dynamical observables (see Section II and shadowed rectangles in Figure 3). Hence, contrary to the findings of Ref. [31], we conclude that microlensing observations and data on the rotation curve of the Milky Way are perfectly compatible with the findings of N -body simulations in ΛCDM cosmologies. Nonetheless, interesting constraints may be

placed on the slope of the DM profile in our Galaxy: for the fiducial density $\rho_0 = 0.4 \text{ GeV/cm}^3$, Figure 3 excludes $\alpha \gtrsim 1.5$ ($\alpha \lesssim 0.06$) for the generalised NFW (Einasto) profile. Notice that in the NFW (Einasto) case one can set an upper (a lower) limit on α – this is simply because for $r \ll r_s$, $\partial \log \rho_{DM} / \partial \log r = -\alpha$ for NFW and $\partial \log \rho_{DM} / \partial \log r = -2(r/r_s)^\alpha$ for Einasto. Therefore, unlike in the NFW case, a larger α for the Einasto profile corresponds to a faster roll of the slope to 0 as $r \rightarrow 0$ and thus a less steep profile.

Deviations from spherical symmetry can in principle affect the constraints. By modelling an NFW oblate halo as detailed in Section II, we obtain the exclusion curve labelled “q=0.7” in Figure 3 (left) for the case of model 1: at first glance this constraint appears weaker than the spherical one, but it should be noted that an oblate profile corresponds to a higher ρ_0 (about 20% higher according to [52]). Departures from spherical symmetry are therefore not able to weaken significantly our constraints.

Up to now we have fixed the scale radius, galactocentric distance and local circular velocity to the respective fiducial values, $r_s = 20 \text{ kpc}$, $R_0 = 8.0 \text{ kpc}$, $v_0 = 230 \text{ km/s}$. These astrophysical parameters, whose uncertainties are sizeable, affect in distinct ways our calculations. The scale radius r_s , for instance, sets the concentration of the DM profile; the smaller r_s the larger the DM contribution to the rotation curve. On the other hand, a smaller R_0 shrinks the bulge and the disk leading to an increase in the bulge central density to produce the same optical depth; however, a smaller R_0 also leads to a less constraining v_c data set so that overall the larger R_0 the more aggressive our DM constraints. The local circular velocity v_0 , instead, sets essentially the plateau of the rotation curve and thus tighter constraints result for smaller v_0 .

In view of these considerations and using the ranges for r_s , R_0 and v_0 outlined in Sections II and IV ($r_s = 20_{-10}^{+15} \text{ kpc}$, $R_0 = 8.0 \pm 0.5 \text{ kpc}$, $v_0 = 230 \pm 30 \text{ km/s}$), we define three astrophysical setups: (i) conservative, with $r_s = 35 \text{ kpc}$, $R_0 = 7.5 \text{ kpc}$, $v_0 = 260 \text{ km/s}$; (ii) mean, with $r_s = 20 \text{ kpc}$, $R_0 = 8.0 \text{ kpc}$, $v_0 = 230 \text{ km/s}$; and (iii) aggressive, with $r_s = 10 \text{ kpc}$, $R_0 = 8.5 \text{ kpc}$, $v_0 = 200 \text{ km/s}$. The mean configuration was used in Figures 2 and 3. Figure 4 shows the effect of adopting the conservative or aggressive setups on the derived DM upper limits for the generalised NFW profile. For simplicity we only show the upper limits encompassed by all models, instead of individual constraints. We see from this Figure that, for reasonable local DM densities, an NFW profile in line with the findings of numerical simulations can only be (barely) excluded at the expenses of pushing some astrophysical parameters to somewhat extreme values (in particular $v_0 = 200 \text{ km/s}$). We are thus led to the conclusion that the results of Ref. [31] do not hold, given the available microlensing and dynamical data and our present knowledge on astrophysical parameters such as r_s , R_0 or v_0 .

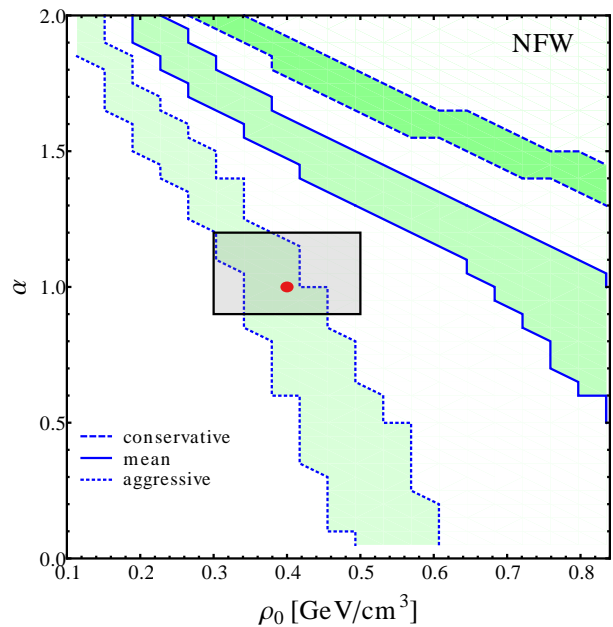


FIG. 4: The bracketing of the 2σ upper limits on the Dark Matter distribution parameters ρ_0 and α for the generalised NFW profile and three astrophysical setups: conservative (dashed; $r_s = 35 \text{ kpc}$, $R_0 = 7.5 \text{ kpc}$, $v_0 = 260 \text{ km/s}$), mean (solid; $r_s = 20 \text{ kpc}$, $R_0 = 8.0 \text{ kpc}$, $v_0 = 230 \text{ km/s}$) and aggressive (dotted; $r_s = 10 \text{ kpc}$, $R_0 = 8.5 \text{ kpc}$, $v_0 = 200 \text{ km/s}$). The two lines for each setup encompass the upper limits set using the baryonic models 1–5. In particular, the mean shadowed area as well as the shadowed rectangle are the same as in the left frame of Figure 3.

B. Determination of (ρ_0, α)

Models 1–4 include no gas component, which in principle makes the corresponding exclusion curves in Figure 3 conservative. Model 5, instead, includes a gas disk and therefore we can go one step further and ask which DM parameters (ρ_0, α) provide the *best fit* to the measured rotation curve.

The results of this fitting procedure are shown by the contours (corresponding to $\Delta\chi^2 = 2.30, 6.18$ for a two-parameters fit) in Figure 5: for DM parameters inside the contours, model 5 manages to explain both the microlensing optical depth towards the bulge and the rotation curve of our Galaxy. It is interesting (and reassuring) that the contours fall nicely on top of the expected ranges indicated by the shadowed rectangles. In particular, we find

$$\rho_0 = 0.20 - 0.55 \text{ GeV/cm}^3 \quad (16)$$

at 1σ for both generalised NFW and Einasto, which is consistent with previous estimates obtained with different techniques [42, 51].

We have also tested the adiabatic contraction model of Ref. [57] (outlined in Section II and equation (8)) in the case of the NFW profile. Using once again model

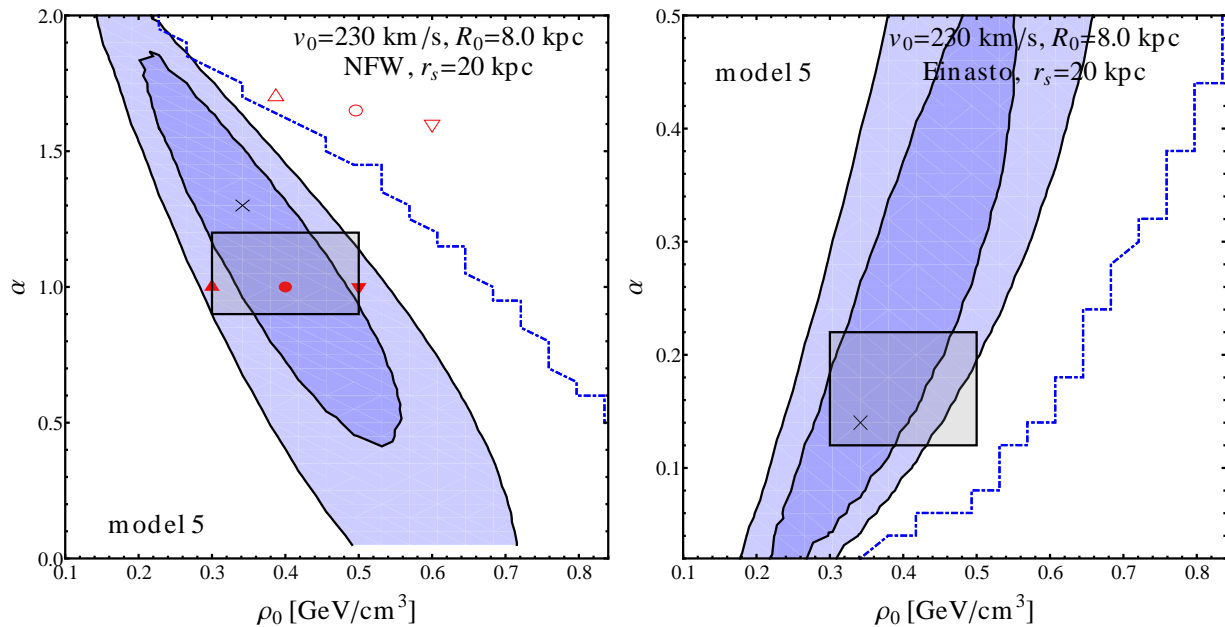


FIG. 5: Constraints on the Dark Matter distribution parameters ρ_0 and α for a generalised NFW (left) and an Einasto (right) profile using the baryonic model 5. The thick dot-dashed curve is the 2σ constraint already shown in Figure 3, while the contours show the parameter space producing a good fit to the rotation curve ($\Delta\chi^2 = 2.30, 6.18$) with the best-fit configuration indicated by the cross. The shadowed rectangle encompasses the ranges of profile slopes found in numerical simulations and the values of ρ_0 found in the recent literature (see Section II), while the red filled circle in the left frame marks the parameter set ($\rho_0 = 0.4 \text{ GeV/cm}^3, \alpha = 1.0$) used to produce Figure 2. The empty up-triangle, circle and down-triangle in the left frame show the local density and shape of the DM profile upon adiabatic contraction of the initial profile indicated by the corresponding filled symbols. The adiabatic contraction was applied using model 5 to fix the baryonic distribution $M_b(< r)$, that entails $f_b = 5.2\%, 4.0\%, 3.0\%$ for the up-triangle, circle and down-triangle, respectively. In both frames we have fixed $r_s = 20 \text{ kpc}$, $R_0 = 8.0 \text{ kpc}$ and $v_0 = 230 \text{ km/s}$.

5 for the baryonic component, we have contracted the initial profiles indicated in Figure 5 (left) by the filled up-triangle, circle and down-triangle with $f_b = M_b(< 200 \text{ kpc})/M_{tot}(< 200 \text{ kpc}) = 5.2\%, 4.0\%, 3.0\%$, respectively. The final DM profile turns out to be well fitted by a generalised NFW function with parameters marked by the empty symbols in the same Figure (the contracted profile corresponding to the filled circle is indicated by the red long-dashed line in the bottom right frame of Figure 2). In particular, we find enhanced local DM densities and slopes $\alpha \simeq 1.6 - 1.7$, which are slightly above the value $\alpha = 1.5$ found elsewhere [73] (see also references therein) but note that we are using the original adiabatic contraction model [57] and not one of its refinements [58, 59]. Although our analysis cannot rule out the presence of adiabatically compressed profiles since they depend on the initial total mass distribution and on the specific baryonic model adopted, it definitely allows us to claim that if the present-day DM profile is steeply rising towards the centre, then the local DM density must be small. For the specific case of $\alpha = 1.5$ (1.7) we find an 1σ range $\rho_0 \simeq 0.25 - 0.35$ ($0.22 - 0.30$) GeV/cm^3 . Some of the extreme models discussed in the literature, e.g. in the context of indirect DM searches [73, 74], are therefore found to be ruled out by a combination of microlensing and dynamical observations.

VI. CONCLUSIONS

We have studied the constraints that microlensing and dynamical observations can set on the distribution of Dark Matter in the Galaxy, keeping into account all experimental uncertainties. Starting from state-of-the-art models for the galactic baryonic component, we have rescaled them to match the observed microlensing optical depth towards the galactic bulge, and compared the resulting rotation curve with the one inferred from terminal velocities of gas clouds and other kinematical probes.

This allowed us to revisit the compatibility of different observational probes with the results that emerge from numerical simulation in ΛCDM cosmologies. We have followed two different approaches. In the first one, we have set conservative upper limits on the Dark Matter local density and profile shape towards the centre of the Galaxy, working with generalised NFW and Einasto profiles. The fiducial parameters usually adopted in the literature for both profiles have been found to be safely within the allowed regions set by our analysis, contrary to earlier claims of inconsistency between observations and cuspy Dark Matter profiles.

In our second approach, we focussed on the only baryonic model among those discussed here that also contains

a description of the amount and distribution of gas, which is expected to provide a non-negligible contribution to the mass and therefore to the rotation curve of the Milky Way. For this specific model, we were able to calculate the values of the Dark Matter parameters that provide the best fit to the combination of microlensing and rotation curve data. The resulting 1σ range for the local DM density, for both the Einasto and NFW profiles, was found to be $\rho_0 = 0.20 - 0.55 \text{ GeV/cm}^3$, therefore consistent with estimates obtained in the literature with different techniques.

Finally, we have studied the consequences of adiabatic compression, often invoked as a mechanism that could increase the amount of Dark Matter in the innermost regions of the Galaxy, and found that although our analysis is not able to discard this mechanism in general, it rules out combinations of local densities and profile slopes invoked in the literature, e.g. in the context of indirect Dark Matter searches. For $\alpha = 1.5$ (1.7) we constrain the local DM density to be within the 1σ range $\rho_0 \simeq 0.25 - 0.35$ ($0.22 - 0.30$) GeV/cm^3 .

As numerical simulations that include the effect of baryons become ever more accurate and reliable, it will

be interesting to compare the findings of these simulations with the wealth of observational data that are currently available. In particular, these simulations should allow us to tie together the distribution of baryons and Dark Matter, and to provide a more precise prescription for the slope of the DM profile towards the galactic centre. This slope is currently extrapolated from simulations *without* baryons, which is an unreliable procedure given that baryons are known to dominate the gravitational potential in the inner Galaxy.

Acknowledgements: We would like to thank Sebastiano Calchi Novati, Juerg Diemand and Michael Kuhlen for helpful discussions. F.I. is supported from the European Community research program FP7/2007/2013 within the framework of convention #235878, and acknowledges the hospitality of the Institute for Theoretical Physics at the University Zürich. M.P. acknowledges the support from Fundação para a Ciência e Tecnologia (Ministério da Ciência, Tecnologia e Ensino Superior) in the early stages of this work, and from the Swiss National Science Foundation in the later ones.

-
- [1] L. Bergstrom and A. Goobar, *Cosmology and particle astrophysics* (Berlin, Germany: Springer, 2004), 364 p.
 - [2] G. Bertone, D. Hooper and J. Silk, *Phys. Rept.* 405 (2005) 279, hep-ph/0404175.
 - [3] *Particle Dark Matter: Observations, Models and Searches* (Cambridge, UK: Cambridge University Press, 2010), edited by Gianfranco Bertone.
 - [4] J. Diemand et al., *Nature* 454 (2008) 735, 0805.1244.
 - [5] <http://www.ucolick.org/~diemand/vl/index.html>.
 - [6] V. Springel et al., *Mon. Not. Roy. Astron. Soc.* 391 (2008) 1685, 0809.0898.
 - [7] <http://www.mpa-garching.mpg.de/aquarius/>.
 - [8] L.E. Strigari and R. Trotta, *JCAP* 0911 (2009) 019, 0906.5361.
 - [9] A.M. Green, (2010), 1004.2383.
 - [10] C. McCabe, *Phys. Rev. D* 82 (2010) 023530, 1005.0579.
 - [11] M. Pato et al., *Phys. Rev. D* 83 (2011) 083505, 1012.3458.
 - [12] M. Vogelsberger et al., (2008), 0812.0362.
 - [13] L. Pieri et al., *Phys. Rev. D* 83 (2011) 023518, 0908.0195.
 - [14] B. Paczynski, *Astrophys. J.* 304 (1986) 1.
 - [15] M. Kiraga and B. Paczynski, *Astrophys. J. Lett.* 430 (1994) L101.
 - [16] Supernova Cosmology Project, C. Alcock et al., *Nature* 365 (1993) 621.
 - [17] E. Aubourg et al., *Nature* 365 (1993) 623.
 - [18] A. Udalski et al., *Acta Astron.* 43 (1993) 289.
 - [19] E.I. Gates, G. Gyuk and M.S. Turner, *Phys. Rev. Lett.* 74 (1995) 3724, astro-ph/9411073.
 - [20] A. Udalski et al., *Acta Astron.* 44 (1994) 165, astro-ph/9407014.
 - [21] T. Sumi et al., *Astrophys. J.* 636 (2006) 240, astro-ph/0502363.
 - [22] C. Alcock et al., *Astrophys. J.* 541 (2000) 734, astro-ph/0002510.
 - [23] MACHO Collaboration, P. Popowski et al., *Astrophys. J.* 631 (2005) 879, astro-ph/0410319.
 - [24] The EROS Collaboration, C. Afonso et al., *Astron. Astrophys.* 404 (2003) 145, astro-ph/0303100.
 - [25] C. Hamadache et al., *Astron. Astrophys.* 454 (2006) 185, astro-ph/0601510.
 - [26] Y.R. Rahal et al., *Astron. Astrophys.* 500 (2009) 1027, 0901.1325.
 - [27] T. Sumi et al., *Astrophys. J.* 591 (2003) 204, astro-ph/0207604.
 - [28] M. Moniez, *Gen. Rel. Grav.* 42 (2010) 2047, 1001.2707.
 - [29] Y. Sofue, M. Honma and T. Omodaka, (2008), 0811.0859.
 - [30] K. Kuijken, (1997), astro-ph/9706054.
 - [31] J.J. Binney and N.W. Evans, *Mon. Not. Roy. Astron. Soc.* 327 (2001) L27, astro-ph/0108505.
 - [32] P. Popowski et al., (2000), astro-ph/0005466.
 - [33] D.J. Majaess, D.G. Turner and D.J. Lane, *Mon. Not. Roy. Astron. Soc.* 398 (2009) 263, 0903.4206.
 - [34] S. Gillessen et al., *Astrophys. J.* 692 (2009) 1075, 0810.4674.
 - [35] M. Reid, *Ann. Rev. Astron. Astrophys.* 31 (1993) 345.
 - [36] IAU, XIXth General Assembly (1985), http://www.iau.org/static/resolutions/IAU1985_French.pdf.
 - [37] E. Dwek et al., *Astrophys. J.* 445 (1995) 716, Fermilab Library Only.
 - [38] K. Stanek et al., (1995), astro-ph/9508008.
 - [39] N.J. Rattenbury et al., *Mon. Not. Roy. Astron. Soc.* 378 (2007) 1064, 0704.1614.
 - [40] S. Novati et al., *Astron. Astrophys.* 480 (2008) 723, 0711.3758.
 - [41] H. Zhao, *Mon. Not. Roy. Astron. Soc.* 283 (1996) 149, astro-ph/9512064.
 - [42] R. Catena and P. Ullio, *JCAP* 1008 (2010) 004, 0907.0018.

- [43] E. Gardner and C. Flynn, *Mon.Not.Roy.Astron.Soc.* 405 (2010) 545, 1002.0551.
- [44] E. Gardner et al., (2010), 1009.4190.
- [45] D. Pfenniger, *Astron.Astrophys.* 134 (1984) 373.
- [46] C. Han and A.P. Gould, *Astrophys.J.* 592 (2003) 172, astro-ph/0303309.
- [47] J.F. Navarro et al., (2008), 0810.1522.
- [48] J.F. Navarro et al., *Mon.Not.Roy.Astron.Soc.* 349 (2004) 1039, astro-ph/0311231.
- [49] E. Hayashi and S. White, (2007), 0709.3933.
- [50] L. Gao et al., (2007), 0711.0746.
- [51] P. Salucci et al., *Astron. Astrophys.* 523 (2010) A83, 1003.3101.
- [52] M. Pato et al., *Phys. Rev. D*82 (2010) 023531, 1006.1322.
- [53] A.V. Maccio', A.A. Dutton and F.C.d. Bosch, (2008), 0805.1926.
- [54] L. Bergstrom, P. Ullio and J.H. Buckley, *Astropart. Phys.* 9 (1998) 137, astro-ph/9712318.
- [55] V.P. Debattista et al., (2007), 0707.0737.
- [56] O. Agertz, R. Teyssier and B. Moore, (2010), 1004.0005.
- [57] G.R. Blumenthal et al., *Astrophys. J.* 301 (1986) 27.
- [58] O.Y. Gnedin et al., *Astrophys. J.* 616 (2004) 16, astro-ph/0406247.
- [59] M. Gustafsson, M. Fairbairn and J. Sommer-Larsen, *Phys. Rev. D*74 (2006) 123522, astro-ph/0608634.
- [60] H. Zhao and S. Mao, (1996), astro-ph/9605030.
- [61] A. Klypin, H. Zhao and R.S. Somerville, *Astrophys. J.* 573 (2002) 597, astro-ph/0110390.
- [62] W. Dehnen and J. Binney, *Mon. Not. Roy. Astron. Soc.* 294 (1998) 429, astro-ph/9612059.
- [63] T. Sumi et al., *Nature* 473 (2011) 349, 1105.3544.
- [64] J. Binney and T. Scott, *Galactic Dynamics* (Princeton, USA: Princeton University Press, 2008).
- [65] S. Malhotra, *Astrophys. J.* 433 (1994) 687, arXiv:astro-ph/9404028.
- [66] S. Demers and P. Battinelli, *Astron.Astrophys.* 473 (2007) 143.
- [67] L. Blitz, M. Fich and A.A. Stark, *Astrophys. J. Suppl.* 49 (1982) 183.
- [68] SDSS, X.X. Xue et al., *Astrophys. J.* 684 (2008) 1143, 0801.1232.
- [69] Y. Sofue, (2008), 0811.0860.
- [70] M.J. Reid et al., *Astrophys. J.* 700 (2009) 137, 0902.3913.
- [71] J. Bovy, D.W. Hogg and H.W. Rix, *Astrophys. J.* 704 (2009) 1704, 0907.5423.
- [72] P.J. McMillan and J.J. Binney, (2009), 0907.4685.
- [73] G. Bertone and D. Merritt, *Phys. Rev. D*72 (2005) 103502, astro-ph/0501555.
- [74] G. Bertone and D. Merritt, *Mod.Phys.Lett. A*20 (2005) 1021, astro-ph/0504422.